CORE-SHELL NANOFIBERS INTEGRATING GROWTH FACTOR-LOADED NANOPARTICLES FOR SPATIO-TEMPORAL DELIVERY IN CHRONIC WOUND HEALING

Ovidio Catanzano[1*], Irene Bonadies[1], Clara Gamba[1], Michele Guida[2],
Gennaro Roberto Abbamondi[3], Giuseppina Tommonaro[3], Hossam Ahmed[4],
Fabiana Quaglia[2], Joshua S. Boateng[4*]

[1]Institute for Polymers, Composites and Biomaterials (IPCB-CNR), Via Campi Flegrei 34, 80078 Pozzuoli, NA, Italy;

[2] Department of Pharmacy, University of Napoli Federico II, Via Domenico Montesano 49, 80131 Napoli, Italy;

[3]Institute of Biomolecular Chemistry (ICB-CNR), Via Campi Flegrei, 34, 80078 Pozzuoli, NA, Italy

[4]School of Science, Faculty of Engineering and Science, University of Greenwich, Medway, Central Avenue, Chatham Maritime, ME4 4TB, Kent, UK.

*ovidio.catanzano@cnr.it

**J.S.Boateng@greenwich.ac.uk*

ABSTRACT

Effective chronic wound management increasingly relies on advanced delivery systems capable of providing spatio-temporal control over release of therapeutic agents. Such systems can localize treatment precisely at the wound site while coordinating the multiple bioactive cues, addressing the complex and sequential biological processes required for successful tissue repair. In this study, we present a composite core–shell nanofiber dressing designed to integrate EGF-loaded nanoparticles (NPs) and ciprofloxacin, addressing two key requirements of wound healing: rapid antimicrobial protection and promotion of tissue regeneration. Fabricated via a green coaxial electrospinning approach under aqueous conditions, the system features a polyvinyl alcohol core and a polyvinylpyrrolidone /hyaluronic acid shell. Nanoencapsulation was employed to protect the growth factor from harsh processing conditions and to enable precise delivery of EGF directly to the wound site. EGF loaded NPs with an average diameter of around 170 nm were prepared by modified solvent diffusion and loaded into a nanofiber shell layer by dispersion in the polymeric solution. The successful formation of the core-shell architecture and homogeneous NPs loading was confirmed by TEM and confocal microscopy. Upon contact with wound exudate, the nanofiber dressing outer shell rapidly dissolves, enabling a fast release of EGF-loaded NPs, while simultaneously triggering sustained ciprofloxacin release from the core, enabling coordinated dual therapeutic delivery. The dressing exhibited antibacterial activity against both Gram-positive and Gram-negative bacteria, showed high biocompatibility and promoted effective *in vitro* wound closure in a scratch assay. By combining multiple encapsulation techniques, this dressing architecture enabled spatial segregation of therapeutic agents within the core and shell allowing coordinated and temporally controlled delivery at the wound site. We expect that this approach may support localized treatment, minimize off-target effects, and protect surrounding healthy tissue, potentially addressing the complex requirements of chronic wound healing and highlighting the promise of rationally engineered core–shell platforms for advanced wound care.

KEYWORDS

Wound dressing; PLGA nanoparticles; Epidermal growth factor; Core-shell nanofibers.

GRAPHICAL ABSTRACT

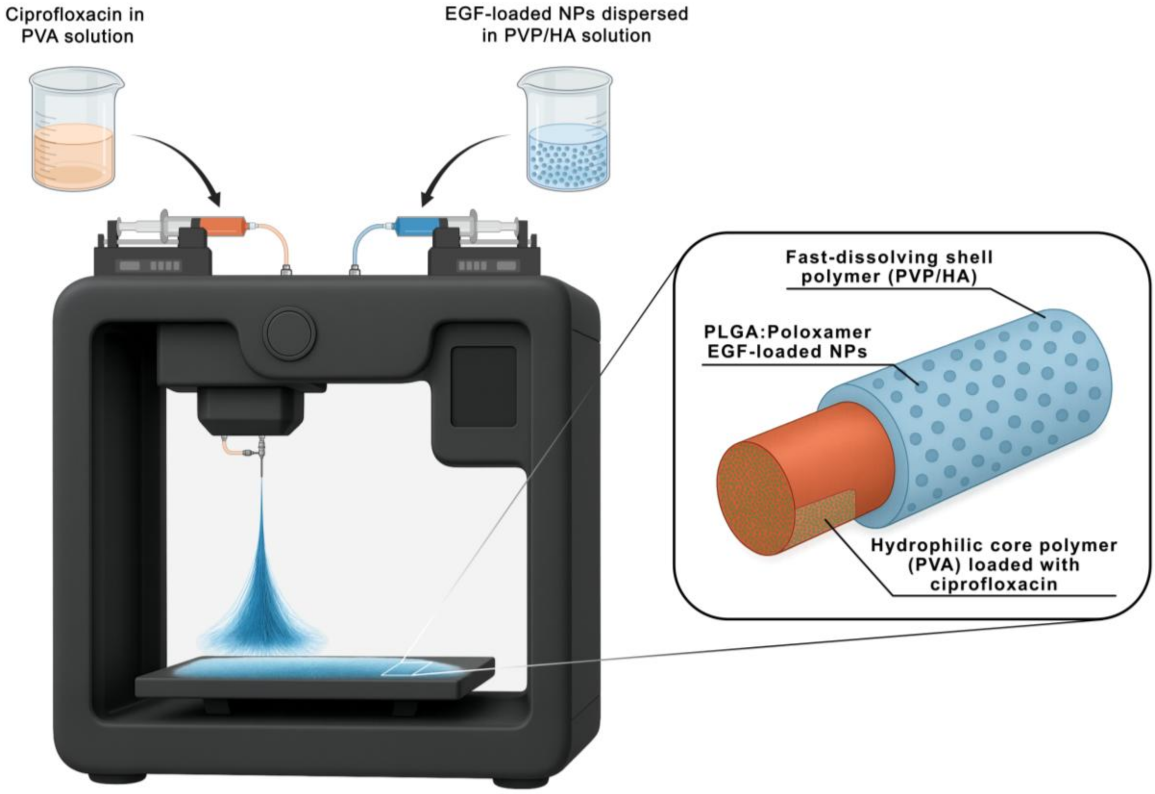

1. INTRODUCTION

Wound healing is a complex, dynamic process often disrupted in chronic conditions such as diabetes or infection-prone environments. While traditional wound dressings provide a physical barrier, they typically cannot enhance the wound healing process.[1] Recent advances in biomaterials have opened new avenues for designing smart and therapeutic wound dressings that not only protect but also actively take part in the healing process by delivering therapeutic agents in a controlled and sustained manner.[2-5] Wound dressings offer an effective platform for the localized delivery of therapeutic entities such as antimicrobial agents and growth factors (GFs), enabling controlled release directly at the wound site and minimizing unwanted side effects or exposure to healthy tissues.[1, 6] Additionally, by engineering the scaffold structure, it is possible to achieve a temporally regulated release profile, ensuring that the bioactive molecules remain within therapeutic concentrations for durations aligned with the different physiological stages of tissue repair.

Polymer-based electrospun nanofibers (NFs) have gained significant attention as efficient drug delivery platforms, due to their capacity to directly incorporate therapeutic agents and provide a prolonged and controlled release profile.[7-10] The technique's compatibility with a wide range of polymer systems, along with its precise control over NFs morphology and cost-effective processing, makes it an ideal candidate for the development of next generation wound dressings.[7, 11, 12] NFs dressings combine excellent mechanical flexibility, conformability, breathability, with a high surface-area-to-volume ratio, making them particularly effective in meeting the dual demands of functionality performance and structural integrity in chronic wound management.[1, 9, 13] Furthermore, electrospun NFs can reduce the frequency of application and help preserve the stability and bioactivity of incorporated therapeutic agents.[1, 7, 12, 14] Finally, their diameters, typically below 1000 nm, closely resemble those of Type I collagen fibers in the dermis (50–500 nm), allowing them to effectively mimic the architecture of the skin's extracellular matrix (ECM) and support tissue regeneration.[15, 16] However, the harsh electrospinning processing conditions, including high voltage and solvent exposure, pose significant challenges for encapsulating delicate bioactive compounds such as GFs, potentially leading to their denaturation and loss of functionality.[6]

Coaxial electrospinning is a specialized technique that offers distinct advantages for drug delivery applications. The core–shell architecture allows compartmentalized encapsulation of multiple bioactive agents, while the high surface area-to-volume ratio of the resulting NFs provides extensive contact with the surrounding environment, promoting efficient and controlled drug release. Moreover, this architecture allows independent modulation of release kinetics and supports high drug loading and encapsulation efficiency, making coaxial NFs particularly attractive for sustained therapeutic delivery. Notably, coaxial electrospinning maintains the separation of core and shell polymer solutions until ejection, enabling the combination of distinct, or even opposing, material properties within a single fiber. This feature facilitates the fabrication of multifunctional wound dressings that integrate the complementary benefits of both components.[17] Xu and coworkers,[18] identified the unique advantages of electrospun NFs that make them versatile biomaterials in regenerative medicine (e.g. wound healing, tissue regeneration and immune modulation). Their functional characteristics include possessing high porosity and surface-to-volume ratio, exhibiting 3D structures similar to the skin's extracellular matrix with resultant improvement in tissue biocompatibility as well as efficient drug loading capacity. The current study employed a co-axial electrospinning to obtain core shell nanofiber architecture which enable the integration of materials with distinct functionalities within a single fiber, thus providing significant versatility in engineering design of a multifunctional dressings with the ability to target different aspects of the complex wound environment as well as wound healing process itself.[10]

Epidermal growth factor (EGF) is a key regulator of wound healing and tissue homeostasis, influencing critical cellular functions such as proliferation, migration, differentiation, and survival.[19] Its long-standing clinical use is attributed to its high efficacy and excellent tolerability. However, to ensure effective therapeutic outcomes, EGF must be delivered through a delivery system that provides sustained stability and protection against proteolytic degradation at the wound site.[20] Nanotechnology-based platforms have emerged as optimal systems for GFs delivery, and their application in wound healing has demonstrated promising outcomes, including enhanced re-epithelialization, collagen fiber deposition, tissue regeneration, and accelerated wound closure in chronic diabetic wounds.[21-23] In particular, poly(lactic-co-glycolic acid) (PLGA) nanoparticles (NPs) are very attractive carriers for the delivery of GFs in wound healing therapies, offering controlled and sustained release while preserving protein stability.[6, 24] As a biodegradable and FDA-approved polymer, PLGA degrades into non-toxic byproducts naturally metabolized by the body, minimizing toxicity concerns. Encapsulation of GFs such as vascular endothelial growth factor (VEGF) and basic fibroblast growth factor (bFGF) within PLGA NPs enables a sustained release profile, maintaining therapeutic concentrations over extended periods and reducing the need for frequent administrations.[25-27]

The complexity of the wound healing process, along with the variability among chronic wound types, necessitates a tunable, multi-targeted approach in which multiple bioactive agents are delivered simultaneously to address different phases of healing.[6] In this context, combining antimicrobial strategies with regenerative cues is particularly promising, as it both controls infection and promotes tissue regeneration, ultimately accelerating wound healing. Recent studies have highlighted the potential of multifunctional wound dressings that integrate antimicrobial activity with tissue regeneration.[28-30] Such systems not only prevent bacterial infection but also promote fibroblast proliferation, angiogenesis, and extracellular matrix deposition, providing a comprehensive approach to accelerate chronic wound healing. More recently, Schulte-Werning and co,[31] reported the development of core–shell nanofiber dressings embedding chloramphenicol-loaded liposomes for the treatment of infected wounds, further underscoring the potential of this approach to generate bioactive scaffolds capable of actively participating in the wound healing process.

In this work, we designed and fabricated a multicomponent core–shell NFs system specifically engineered to address multiple factors that hinder wound healing. The platform integrates an antibiotic within the fiber core and EGF-loaded PLGA NPs in the outer shell enabling precise compartmentalization of therapeutics and complementary release profiles. Ciprofloxacin (Cip), an antibiotic known for its strong antimicrobial efficacy in treating complicated wound infections and for its favorable clinical outcomes in managing severe skin and soft tissue infections,[32] was incorporated to provide robust and sustained antibacterial protection. Core–shell NFs composed of polyvinyl alcohol (PVA) hyaluronic acid (HA), polyvinylpyrrolidone (PVP) were fabricated entirely using aqueous solutions, avoiding toxic organic solvents and preserving the bioactivity of both Cip and the encapsulated EGF-loaded NPs. This green fabrication strategy improves biocompatibility, enhances safety, and supports the development of next generation wound dressings. By combining Cip in the core with EGF-loaded NPs in the shell, this architecture enables spatially organized and synergistic in situ delivery, highlighting the potential of core–shell NFs as multifunctional systems for advanced wound management. We propose that this design supports a coordinated therapeutic approach, integrating rapid antimicrobial activity with sustained tissue regeneration, thereby addressing the complex and multifactorial challenges of chronic wound healing.

2. EXPERIMENTAL

2.1. Materials

The GMP grade PLGA PURASORB® PDLG 5002 (uncapped PLGA 50:50, inherent viscosity 0.2 dL/g) was purchased from Corbion (Netherlands). Rhodamine-labeled PLGA (lactide:glycolide 50:50, Mn 10,000-30,000), Kolliphor P188 (poloxamer F-68), human serum albumin (HSA), heparin (Hp) sodium salt, Mowiol® 4-88 (Average Mw~31,000 g/mol), trehalose, and PBS were purchased from Merck KGaA (Germany). For NFs production, polyvinyl alcohol (PVA; average Mw ~89,000–98,000 g/mol) and polyvinylpyrrolidone (PVP; average Mw ~360,000 g/mol) were purchased from Merck KGaA (Germany) and used as received. Mannitol was purchased from Roquette (France). The ISO 9001 certified hyaluronic acid (HA; average Mw 8.0 x 10^5 g/mol) used in this study was a kind gift from Altergon Italia S.r.l (Italy). Ethanol 96% (v/v) was supplied by Carlo Erba Reagents (Italy). All the other chemicals were of analytical reagent grade with the highest purity available. Ultrapure water (Milli-Q grade) was used for all experiments.

2.2. Preparation of EGF-Loaded NPs

NPs were prepared by a modified solvent diffusion technique with a fixed PLGA:poloxamer mass ratio of 1:1 as previously described.[33] Briefly, 15 mg of poloxamer F68 and 15 mg of PLGA RG 503 were dissolved in 1 mL of methylene chloride by vortex mixing. An aqueous solution (100 µL) containing 5 µg of EGF and the two stabilizing agents, heparin (5 µg) and HSA (200 µg), was prepared, added to the polymer solution, and emulsified by vortex mixing for 30 seconds. The resulting emulsion was quickly added to 12.5 mL of ethanol, resulting in the immediate precipitation of the polymer in the form of NPs.The dispersion was diluted with 12.5 mL of Mowiol® 4-88 (0.1% w/v) and stirred at room temperature in a fume hood for 10 minutes. Afterwards, the organic solvents were eliminated through evaporation under vacuum at 30°C (Rotavapor, Heidolph VV 2000, Germany). To remove any unencapsulated EGF, the aqueous dispersion was dialyzed for 1 hour using a Pur A-Lyzer™ dialysis tube (pore size 3.5 kDa; Merck KGaA, Germany) against ultrafiltered water under mild stirring. The external ultrafiltered water was changed every 15 minutes.

Fluorescent NPs (NPs-Rhod) were prepared using the same method, with rhodamine-labeled PLGA incorporated at 10% (w/w) of total PLGA. NPs-Rhod were employed to assess their integration in and release from the core–shell NFs.

A freeze-drying method was optimized for drying the PLGA:poloxamer NPs containing EGF to improve their stability, facilitate storage and handling, and allow easy redispersion prior to use. Trehalose and mannitol were evaluated as cryoprotectants at concentrations of 5% and 10% (w/v). The total volume of the NP suspension was adjusted to 3 mL with filtered water to obtain a theoretical NPs concentration of 10 mg/mL. The cryoprotectant powder was added to the suspension and dissolved by vortexing for 1–2 minutes. The resulting mixtures were frozen at −20 °C and subsequently lyophilized at 0.01 atm and 20 °C using a Lyovapor L-200 laboratory freeze dryer (Buchi, Switzerland). The lyophilized NPs were reconstituted in 1 mL of ultrapure water and analyzed to determine particle size and PDI after the lyophilization process.

2.3. Characterization of EGF-Loaded NPs

The average hydrodynamic diameter (D_H), and polydispersity index (PDI) of the NPs were determined by dynamic light scattering (DLS) using a Zetasizer® Nano-ZS ZEN 3600 (Malvern, UK) equipped with a red laser light beam (λ=632.8 nm). With the same apparatus, the zeta potential was calculated from the electrophoretic mobility values determined by laser Doppler anemometry (LDA). Results are reported as the mean of three separate measurements of three different batches ± SD (n = 9).

The yield of the NPs production process was evaluated gravimetrically by weighing the solid residue recovered after freeze-drying the NP dispersion.

The morphology of the optimized NPs systems was observed using Transmission Electron Microscopy (TEM). For TEM analysis, a drop of each sample was deposited on a copper grid and stained with a 2% (w/v) phosphotungstic acid solution. After 30 seconds of staining the grids were washed 3x with milliQ water and allowed to dry under vacuum for approximately 1 hour. A FEI Tecnai G12 microscope equipped with an FEI Aquila 4K CCD camera (Eindhoven, Netherlands) was used for the TEM analysis, operating with an acceleration voltage of 120 kV.

To calculate the encapsulation efficiency (EE%) of EGF, the NPs were isolated using ultracentrifugation at 80,000 rpm for 40 minutes at 4 °C in a refrigerated Optima MAX 130K ultracentrifuge (Beckman Coulter). The supernatant obtained was then analyzed using an ELISA assay specifically designed for quantifying EGF (Thermo Fisher Scientific). The assay was performed according to the manufacturer's protocol. A calibration curve for EGF was prepared in water over the concentration range of 2.5 – 250 pg/mL (R^2 = 0.992). The

EE% was determined indirectly by the difference between the total amount of EGF in each formulation (EGF_{tot}) and the amount present in the supernatant (EGF_{surn}).

2.4. Preparation of Polymeric Solutions

PVA solution was obtained by dispersing the polymer in ultrapure water (15% w/v) for about two hours at 80 °C under magnetic stirring. Once a transparent PVA solution was obtained, it was left to cool for at least 30 minutes, or until the room temperature was reached. PVP (12.5% w/v) and HA (0.5% w/v) were dissolved in a mixture of water/anhydrous ethanol 1:1 at RT and stirred for two hours. To prepare the NPs-loaded core-shell electrospun NFs, the NPs were directly dispersed into the PVP/HA solution at a concentration of 12.5 mg NPs/mL and stirred for 1 hour before electrospinning. Cip (0.5% and 1% w/w relative to PVA) was dissolved in the cooled PVA solution under stirring for 15 minutes.

The stability of the NPs within the solvent mixture was evaluated in a 1:1 water/ethanol mixture to simulate the solution in which NPs must be dispersed before the electrospinning process. For this purpose, 0.5 mL of the NP suspension in water was mixed with 0.5 mL of ethanol, and the resulting mixture was transferred to a polypropylene cuvette. Particle size and PDI were measured by DLS at 0, 15, 30, and 45 minutes, and after 1, 1.5, 2, and 3 hours to monitor NP stability over time.

The rheological property of the electrospinning solutions was investigated using a HAAKE RheoStress 6000 rotational rheometer (Thermo Scientific, USA). A parallel plate geometry was employed for the measurements (plate P20 CS L S, plate diameter 35 mm, gap between plates 1 mm, sample volume 0.35 mL).

To optimize the preparation of core–shell NFs, a range of electrospinning parameters were systematically investigated to determine the conditions that produced fibers with the most uniform and defect-free morphology.

2.5. Electrospinning Process

Core–shell NFs were fabricated through a coaxial electrospinning technique using a MECC NF-103 electrospinning system (Fukuoka, Japan). The coaxial spinneret consisted of a special ultra-coaxial nozzle where the inner needle had a diameter of 0.2 mm, and the outer needle had a diameter of 0.8 mm. The prepared PVP/HA and PVA solutions were transferred into two separate syringes, which were then secured to the controlled syringe pump of the electrospinning setup. The polymeric solutions were fed through a coaxial nozzle at flow rates of 0.4 mL/h for PVA and 0.5 mL/h for PVP/HA. A positive voltage of 23 kV was applied, and the working distance between the needle tip and the collector was fixed at 220 mm. An aluminum foil was used as a collector to receive the electrospun NFs. All the electrospinning processes were carried out at 25-30 °C and a relative humidity of 9-15%. The optimization of electrospinning parameters and the condition of polymer solutions were defined by naked-eye observations and confirmed by SEM and TEM analysis. All the electrospun NFs were stored at room temperature, in the dark, and at 35% relative humidity for further characterization.

2.6. Chemical-physical Characterization of Electrospun Nanofibers

2.6.1. Morphology of electrospun nanofibers

The morphology of electrospun NFs was evaluated by a field-emission scanning electron microscopy (FESEM, QUANTA200, FEI, The Netherlands) after sputter-coating with gold–palladium. Samples were preliminarily dried under vacuum to remove any residual solvent traces, then directly placed on metal stubs using a double-sided adhesive tape to preserve the NFs' morphology. ImageJ analysis software (ImageJ, National Institutes of Health, USA) was used to evaluate the diameter and distribution of NFs. For this purpose, at least 50 NFs were measured per sample, using multiple SEM images to ensure representative sampling.

The core–shell morphology was verified by TEM using a Thermo Scientific Talos L120C microscope. Graphene-coated copper TEM grids were gently scratched off the surface of the electrospun mat to collect samples.

Confocal laser scanning microscopy (CLSM) was performed to verify the spatial distribution of the EGF-loaded NPs in the NFs. Imaging was conducted using a Zeiss LSM 700 microscope (Carl Zeiss, Germany) equipped with Argon (488 nm) and HeNe (561 and 639 nm) lasers and a 40×/1.2 NA objective lens.

2.6.2. Fourier transform infrared spectroscopy in attenuated total reflectance mode (FTIR-ATR)

ATR-FTIR spectra of the NFs were acquired using a Thermo Fisher Scientific Nicolet 6700 FTIR spectrometer. Measurements were performed in ATR mode with a resolution of 4 cm^{-1}, averaging 16 scans per spectrum over the range of 4000 to 650 cm^{-1}.

2.6.3. *Thermogravimetric analysis (TGA)*

Thermogravimetric analysis was performed in duplicate using a TA Q5000 analyzer to investigate the thermal stability of the NFs. The sample weight was approximately 5–10 mg and the test procedure involved a ramp from 40 °C up to 700 °C at a constant heating rate of 10°C/min in nitrogen atmosphere.

2.6.4. *Nanofiber behaviors in water*

To investigate the morphological response of the core-shell NFs upon contact with a moist surface, approximately 30 µL of distilled water (pH = 6.5-7.0) was deposited onto the electrospun mat. After 3 minutes of contact, the samples were examined via SEM to evaluate any morphological alterations.

The release of the NPs from the NFs was evaluated by fluorescence using rhodamine-labeled NPs (NPs-Rhod). 10 mg NFs were accurately weighed using an analytical balance and placed in an amber vial containing 3 mL of phosphate buffer saline (PBS, NaCl 120 mM, KCl 2.7 mM, Na2HPO4 10 mM) at pH 7.4. At predetermined time intervals, up to 24 hours, 500 µL of the release medium was carefully withdrawn without disturbing the NFs settled at the bottom of the vial and replaced with an equal volume (500 µL) of fresh PBS. The collected samples were stored in the dark at 4°C in appropriately labeled and sealed Eppendorf microtubes. The fluorescence emission spectra of the NPs-Rhod were collected with a fluorescence spectrometer (RF-6000, Shimadzu Corporation, Tokyo, Japan) at the excitation wavelength of Rhodamine B (λ_{exc} = 553 nm; λ_{em} = 578). A calibration curve for NPs-Rhod was prepared in water, starting from a 0.17 mg/mL solution and making appropriate dilutions, (R^2 = 0.998).

2.6.5. *Mechanical properties*

The mechanical properties of the NFs were evaluated via tensile testing using an INSTRON 5564 testing machine equipped with a 100 N load cell, operated at room temperature (25°C). The NF mats were cut into rectangular-shaped specimens (length: 3 cm, width: 0.5 cm) and mounted on the instrument using standard screw action grips and filter paper to enhance friction and prevent sample slippage during testing. The average thickness of each sample was measured at a minimum of three different points using a digital caliper and recorded in the instrument software. Tensile tests were conducted at a crosshead speed of 10 mm/min, with each sample stretched until failure. Mechanical parameters were calculated as the means of five independent measurements.

2.7. *In Vitro* Drug Release from Nanofibers

The release profiles of EGF and Cip from the drug-loaded NFs were evaluated by the dialysis method. Specifically, a custom-made release system was assembled using a disposable polycarbonate basket (24 mm diameter) with an integrated membrane having 8.0 µm pores at the bottom (Corning Transwell®). Simulated wound fluid (SWF, 0.02 M $CaCl_2$, 0.4 M NaCl, and 0.4 M Trizma™ base) at pH 7.4 was selected as release medium to mimic the composition and osmolarity of the exudate typically found in chronic wounds. The release experiments were carried out in triplicate.

The release of Cip from the NFs was assessed by incubating 20 mg of NFs in 5 mL of simulated wound fluid (SWF) at 37 °C in an oscillating water bath. At predetermined intervals, up to 7 days, 500 µL of the release medium were collected from the bottom of the basket and replaced with an equal volume (500 µL) of fresh medium previously maintained at 37 °C. The Cip released from the NFs was quantified using UV-Vis spectrophotometry. A GENESYS UV-VIS spectrophotometer (Thermo Fisher Scientific™) was set to a wavelength of 282 nm for the measurements. A calibration curve for Cip was prepared in methanol, starting from a 0.01 mg/mL solution and making appropriate dilutions ($R^2 = 0.999$).

The release of EGF from the NFs was assessed using a modified version of the experimental setup previously used for Cip release. In this procedure, 3 mg of NFs were carefully weighed and placed into the release system. Next, 3 mL of SWF were added to ensure that the NFs were fully submerged. At predetermined time intervals, up to 14 days, 200 µL aliquots of the release medium were collected from the bottom of the basket and replaced with an equal volume of fresh release medium. The amount of EGF released was determined using the ELISA assay as described earlier, following the manufacturer's protocol.

The results are reported as the percentage of EGF or Cip released (mean ± standard deviation) calculated from the release measurements obtained for three independent NFs samples.

2.8. Antimicrobial Activity

The antimicrobial activity of core–shell NFs loaded with Cip was evaluated using a modified Kirby–Bauer disk diffusion assay.[34, 35] Circular samples of the NFs (6 mm in diameter) were divided into three experimental groups based on Cip loading: unloaded (0%) and loaded with 0.5% and 1% w/w Cip. As controls, sterile filter paper disks (OXOID, 6 mm diameter) were used, either unloaded or impregnated with Cip solutions delivering 2.2 µg and 4.4 µg of drug, corresponding to the loading of the NFs.

Antibacterial activity was tested against three reference strains: *E. coli* DSM 498 (Gram-negative); *M. luteus* DSM 348 and *B. subtilis* subsp. *spizizenii* DSM 347 (Gram-positive). The strains were stocked on Nutrient Agar (NA) plates stored at 5°C. Prior to testing, cultures were refreshed by overnight incubation at 30 °C in Nutrient Broth (NB); the medium for *B. subtilis* was supplemented with manganese sulphate ($MnSO_4$) to support sporulation and optimal growth.

Bacterial dispersions were adjusted to a 0.5 McFarland turbidity standard (approx. 1×10^8 CFU/mL). Aliquots of 100 µL were evenly spread onto NB-agar plates using sterile spreaders. NFs and control disks were gently placed on the agar surface using sterile tweezers. Plates were incubated at 30 °C, and inhibition zones were recorded after 24 and 48 hours. Each condition was tested in triplicate. Growth inhibition diameters were quantified using ImageJ software.[36]

2.9. Biocompatibility Studies of Nanofiber Membranes

2.9.1. Hemolysis assay

The blood compatibility of the core-shell NFs was evaluated using the hemolysis assay.[37] Fresh human blood was collected from a healthy donor after obtaining informed consent and centrifuged at 1000 g for 10 minutes (Thermo Scientific Heraeus Labofuge 200 Centrifuge, Waltham, MA, USA) to isolate red blood cells (RBCs). The resulting RBC pellet was washed three times with PBS pH 7.4 through repeated centrifugation and was subsequently diluted tenfold in PBS for further use. A 0.5 mL aliquot of the final RBC dispersion was added to 2.5 mg of NFs (1:5 ratio) in microcentrifuge tubes. After incubation at 37 °C for 1 hour, the samples were centrifuged at 1000 g for 10 minutes using a Minispin® centrifuge (Eppendorf, Hamburg, Germany) to remove non-lysed RBCs. The supernatant was then collected, and hemoglobin release was quantified via spectrophotometric analysis at 541 nm. PBS mixed with diluted RBCs served as the negative control (0% hemolysis), while diluted RBCs treated with 50 µL of 1% (w/v) Triton X acted as the positive control (100% hemolysis). Hemolysis was calculated using Eq. 1:

$$Hemolysis\ ratio\ (\%) \frac{OD_s - OD_n}{OD_p - OD_n} \times\ 100 \qquad \text{[Eq. 1]}$$

where OD_s is the absorbance of the sample, OD_n is the absorbance of the negative control, and OD_p is the absorbance of the positive control.

2.9.2. MTT cell viability assay

The effect of dressings on the viability of human dermal fibroblasts (HDFs) was assessed using MTT assay via the indirect contact approach, following a previously reported procedure.[38] Prior to the MTT testing, the NFs were sterilized using UV radiation overnight in a flow cabinet (NU-437-300E, NUAIRE). The sterilized samples were then immersed in 2.5 mL of complete medium and placed in a Heracell 150i CO_2 incubator (Thermo Fisher Scientific, Loughborough, UK) at 37 °C with 5% CO_2. To prevent interference with cell growth caused by direct contact of the dressings with the complete medium, the supernatant was filtered using a 0.2 μm filter. Cultured cells were seeded at a density of 1×10^5 cells/mL in a 96-well microtiter plate, following the recommended ATCC protocol, and incubated overnight at 37 °C with 5% CO_2 for adherence. After 24 hours, the medium was removed and 100 μL of the sterilized sample was added to the wells. The plates were then further incubated for up to 72 hours and at each time point (24, 48 and 72 hours), the cells were treated with 10 μL of MTT reagent, including the blank (medium only). Subsequently, the plates were returned to the incubator for at least 4 hours, or until a visible purple precipitate formed. Following this, the supernatant was washed and 100 μL was added to all wells including the controls, to dissolve the formazan crystals. The plates were incubated for an additional 30 minutes, after which the absorbance was measured at 492 nm using a microplate reader (Multiscan FC, Thermo Fisher Scientific, Loughborough, UK) equipped with SkanIt for Multiscan FC 3.1. Each experiment was conducted in triplicate (n = 3) biologically and repeated three times for each replicate.~~, yielding a total of n = 9.~~ A known toxic compound (Triton-X) was employed as a positive control (CTR+). The percentage of viable cells was calculated using Eq. 2, where At, Ab, 51, and Ac represent the absorbances of the tested samples, medium only, and negative control (untreated cells), respectively.[39]

$$Cell\ viability\ (\%) = \frac{A_t - A_b}{A_c - A_b} \times 100 \qquad \text{[Eq. 2]}$$

2.9.3. *Live and dead assay*

The live and dead assay was performed using LIVE/DEAD^{TM} Cell Imaging Kit (Thermo Fisher Scientific, Cat. No, R37609). The cells were cultured in a multiwell plate with the addition of sterilized NF mat extracts with each formulation tested in three biological replicates (n = 3) with three technical replicates for each formulation. The assay vials were thawed, and one Live Blue vial was mixed with one Dead Green vial, to create 2x stock. The stock was then added to the wells at volumes equal to that of media within the wells. The plates were then incubated at 25 °C for 15 minutes before observation under a fluorescence microscope. Live cells were seen to be blue (fluorescence excitation at 360 nm and emission at 460 nm), while dead cells with membrane damage were seen as green (fluorescence excitation at 504 nm and emission at 523 nm).[40]

2.10. *In Vitro* Wound Healing (Scratch) Assay

For the scratch assay, HDFs were seeded at a concentration of 3×10^5 cells in each well of a 24-well plate with a polymer coverslip bottom for higher optical quality (Ibidi, UK) and allowed to adhere overnight to form a monolayer (100% confluent). The scratch assay is based on creating an artificial wound by mechanically scraping a confluent cell monolayer, thus creating an empty area to be covered by the cells migrating from the edges.[41] Once the scratch was created manually with a pipette tip, the cells were washed with 2 mL PBS, and cell proliferation and migration were stimulated by treating the cell culture with the supernatant of the dressings prepared. Digital images were acquired using a microscope (AE2000 Binocular Moitic, UK) at x10 magnification every 24 hours up to 72 hours. This experiment was performed in three biological replicates (n = 3) with 6 technical replicates within each replicate. The percentage of wound closure was calculated using NIH Image J software.[42]

2.11. Statistical Analysis

All experiments were performed in triplicate, and the results were expressed as the mean ± standard deviation (SD). Statistical analysis was performed using ANOVA or simple t-test and p-values below 0.05 were considered significant. Microsoft Excel was used for general calculations, while GraphPad Prism® 10.2 (GraphPad Software, La Jolla California USA) was used for data plotting.

3. RESULTS AND DISCUSSION

3.1. Design of dual release nanofibers

NFs incorporating GFs represent a promising strategy for the development of advanced wound dressings, particularly for the management of chronic skin wounds.[22] A standard method to obtain GF-loaded NFs involves dispersing the protein directly into the polymer solution before electrospinning. However, this approach poses several challenges, including low loading efficiency, aggregation, and GFs denaturation due to high voltage and exposure to harsh organic solvents. To overcome these limitations, this study employed NPs encapsulation to protect the GFs from production-induced stress during the electrospinning process, while improving their controlled spatial-temporal release. To promote tissue regeneration and accelerate the healing process, EGF was incorporated into the system and encapsulated within PLGA: poloxamer NPs to protect it from the harsh conditions of the electrospinning process. This strategy provides a stabilizing microenvironment that helps preserve EGF's bioactivity and enables controlled release throughout the wound healing process.

The composite NFs were fabricated with a core-shell structure (Fig. 1) using a green electrospinning approach based entirely on aqueous solvents, thereby avoiding toxic organic solvents to prevent potential damage to both the NPs and the GFs. The selection of PVA, PVP, and HA for the fabrication of core–shell NFs was guided by literature evidence and previous successful applications of these materials to prepare electrospun scaffolds for wound healing.[43-46] PVA was selected for the core fiber due to its excellent biocompatibility, water solubility, and ability to form uniform NFs, making it well-suited for encapsulating bioactive agents.[47, 48] PVP was selected for the shell because it is a synthetic polymer widely employed in dosage forms with excellent biocompatibility, hemocompatibility and safety, Moreover, the presence of both hydrophilic and hydrophobic functional groups in its structure allows PVP to dissolve in a broad range of solvents, offering significant formulation flexibility. To further enhance the bioactivity of the shell, HA, a naturally occurring polysaccharide, was incorporated. HA is well known for its structural role in the ECM and its proven effectiveness in promoting wound healing, particularly in chronic and hard-to-heal wounds.[49] This polymer combination enabled the development of a wound dressing designed to fulfill both mechanical and functional requirements.

Our dressing was specifically designed to facilitate the local delivery of GFs at the wound site by embedding EGF-loaded NPs into the outer shell composed of PVP and HA, both of which dissolve quickly upon contact with wound exudate. Upon exposure to the exudate, the shell disintegrates, depositing the EGF-loaded NPs directly onto the wound surface and ensuring their immediate availability for early-phase tissue repair. In parallel, Cip dispersed within the PVA core is gradually released as the wound exudate permeates the polymer matrix, providing sustained antibacterial protection and creating a synergistic environment for infection control and tissue regeneration.

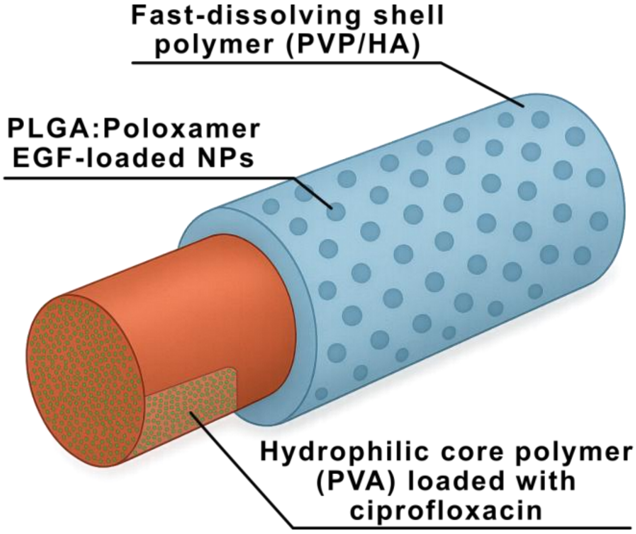

Figure 1. Schematic of the core–shell NFs structure. The fiber core (Orange) contains Cip for sustained antibacterial release, while the outer shell (light blue) incorporates EGF-loaded PLGA NPs releasing GFs. This spatial organization enables coordinated, localized dual delivery directly at the wound site.

3.2. Preparation and Characterization of EGF-Loaded NPs

To protect EGF from the harsh conditions of the electrospinning process, we proposed encapsulating it into PLGA:poloxamer NPs, which were developed as an alternative to conventional PLGA NPs for encapsulating fragile molecules with minimal loss of their biological activity.[50-53] This design enhances the release profile by modifying matrix hydration processes due to the presence of poloxamer, which not only regulates drug release but also prevents the degradation of encapsulated molecules during the release phase. This stability enhancement addresses a common issue with PLGA carriers, where the accumulation of acidic oligomers upon polymer degradation can compromise the integrity of encapsulated protein.[33, 50, 51] PLGA:poloxamer NPs were prepared using the solvent diffusion method, with co-encapsulation of Hp and BSA to stabilize the ternary structure of EGF further and preserve its biological activity.[33, 54] Although EGF lacks intrinsic heparin-binding domains present in other GFs such as VEGF, it can still interact electrostatically with Hp, a process shown to improve its stability and bioactivity.[55, 56] The overall properties of the PLGA:poloxamer NPs are reported in Table 1.

Table 1. Hydrodynamic diameter (D_H), Polydispersity Index (PDI) and ζ -Potential of PLGA:Poloxamer NPs encapsulating different molecules. Encapsulation efficiency (EE %) was evaluated for EGF. Values are reported as mean ± standard deviation from three independent NPs batches (n = 3).

	Encapsulated molecules	***D_H (nm ± SD)***	***PDI***	***ζ Potential (mV ± SD)***	***Production yield (%)***	***EE (%)***
Unloaded NPs	-	167.1 ± 5.0	0.1	-12.9 ± 2.9	89.0 ± 3.4	-
Control NPs	BSA, Hp	158.8 ± 2.2	0.1	-9.6 ± 0.1	75.3 ± 2.5	-
EGF NPs	BSA, Hp, EGF	168.2 ± 9.1	0.1	-8.5 ± 1.6	76.8 ± 7.3	76.5 ± 5.3

In general, PLGA:poloxamer NPs exhibited similar characteristics regardless of the GF and stabilizers encapsulated. All formulations were below 200 nm with a low PDI and monodisperse (Fig. 2A). Encapsulation of EGF in the NPs (9% theoretical loading) was 76.5 ± 5.3 % and the presence of EGF did not affect the colloidal properties of NPs. TEM micrographs confirmed the homogeneous and spherical nature of the prepared EGF-loaded NPs (Fig. 2B and C). Finally, these NPs were freeze-dried, weighed, and dispersed in the nanofiber-forming solution. Our results show that using trehalose (5% w/v) as cryoprotectant, EGF-loaded NPs can be successfully freeze-dried and redispersed with minimal alteration to their colloidal properties (Fig. 2D). These findings indicate that the freeze-drying process preserved both the small particle size and the unimodal size distribution. EGF-loaded NPs maintained their structural integrity and size stability over different contact times in a 1:1 water/ethanol mixture (Fig. 2E). No signs of aggregation or significant changes in particle size were observed, confirming the compatibility of the NPs with the solvent system and their suitability for processing during the electrospinning stage.

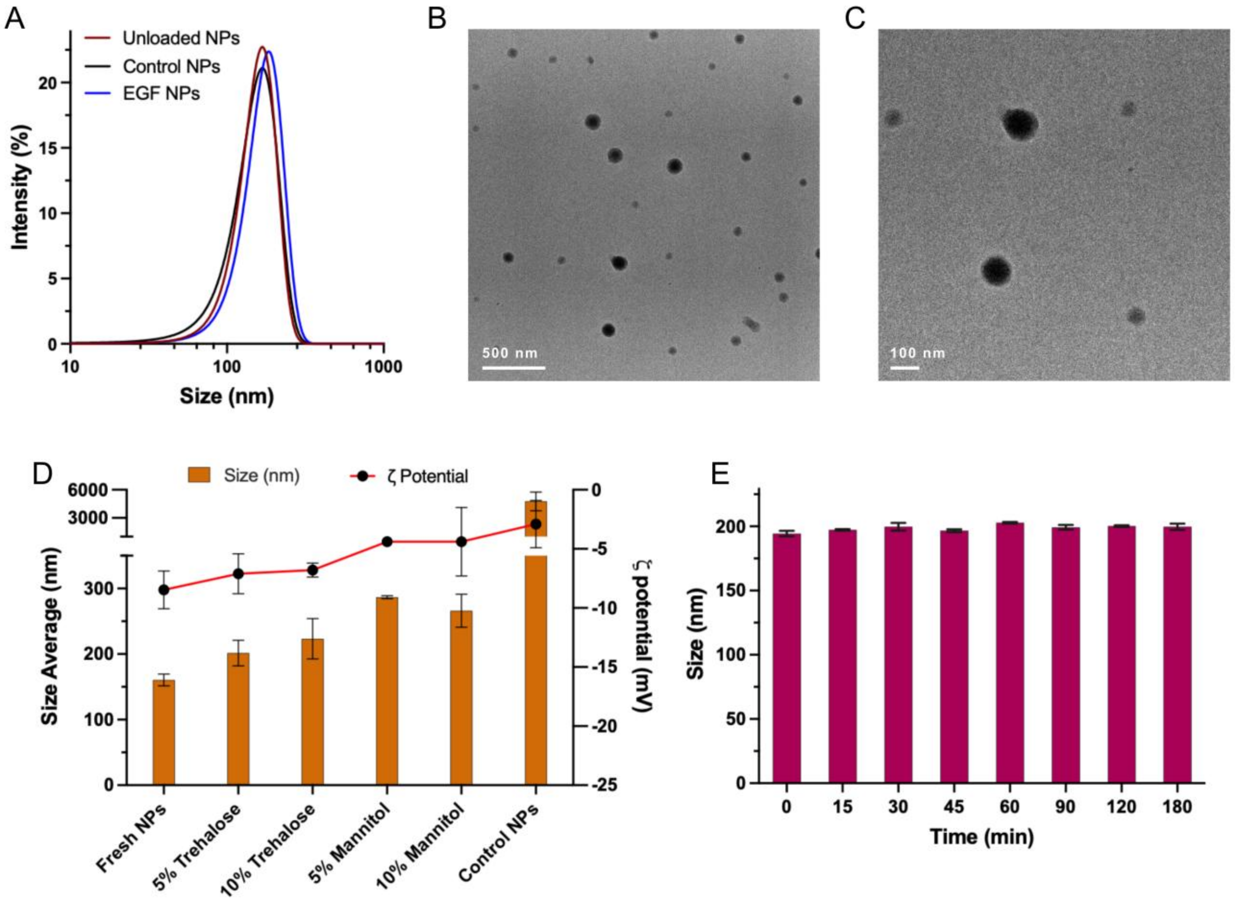

Figure 2. (A) Size distribution of PLGA:poloxamer NPs. (B-C) Representative TEM images of NPs encapsulating BSA, Hp, and EGF (EGF NPs). (D) Particle size and ζ potential after the lyophilization process using different amounts of trehalose and mannitol as cryoprotectants. (E) Particle size of PLGA:poloxamer NPs measured in a 1:1 water/ethanol mixture at different contact times. Results are reported as mean ± standard deviation, based on measurements from three independent NFs samples (n = 3).

3.3. Preparation of Electrospun Nanofibers

Ethanol was used in preparing the PVP/HA solution to improve processability and facilitate rapid drying, ensuring efficient NFs formation without compromising the stability of the NPs or the GFs. The rheological properties of electrospinning solutions are crucial for ensuring stable jet formation, preventing bead formation, and promoting the production of NFs with smooth morphology and homogeneous diameter. Previous studies have shown that interactions between polymers and NPs can influence solution viscosity and consequently, the behavioral characteristics of the electrospinning solutions.[44, 57] In the present study, the rheological properties of the polymeric solutions were evaluated (Table S1), and no significant changes in viscosity were observed, indicating that the incorporation of NPs did not affect the solutions' flow behavior.

The optimal electrospinning conditions for the fabrication of core–shell NFs composed of PVA, PVP, and HA were established through a series of preliminary experiments, as detailed in Supplementary Materials (Section S2). The optimized electrospinning parameters (potential difference 23 mV, collector distance of 220 mm and feeding rates of 0.4 mL/h and 0.5 mL/h for the core and shell solutions, respectively) were found to be suitable for the fabrication of both (A) unloaded (Nf_CS15a) and (B) NPs-loaded NFs (Nf_CS15a-NPs). The NPs were uniformly dispersed in the PVP/HA solution, comprising 1:1 water: ethanol. Cip-loaded NFs were obtained by dissolving the drug directly in the PVA solution, thereby confining it within the core. Both the NPs and Cip-loaded solutions were fully compatible with the previously optimized electrospinning conditions, allowing for efficient NFs production without further adjustments.

The SEM images in Fig. 3A and 3B show that NFs containing EGF-loaded NPs and Cip exhibited no evident morphological differences compared to those prepared without NPs. The nanofibrous scaffold exhibited a uniform and continuous morphology with smooth surfaces and no visible bead formation, confirming a successful electrospinning process. The incorporation of EGF-loaded NPs into the outer shell resulted in a moderate increase in NFs diameter from 252 ± 45 nm to 335 ± 59 nm along with a shift in size distribution toward larger NFs (Fig. 3A-B), reflecting the influence of NP inclusion. The core–shell morphology of the NFs was confirmed by TEM imaging (Fig. 3C), which clearly showed that the PVA core and the embedded NPs were fully enclosed within the outer shell composed of PVP and HA. Minor surface irregularities observed on the NFs can be attributed to the presence of NPs dispersed within the shell layer.

CLSM provided detailed insight into the spatial distribution of NPs within the NFs. NFs incorporating fluorescent PLGA:poloxamer NPs in the shell were imaged to verify the core–shell configuration and assess NP localization. The CLSM images showed a homogeneous red fluorescence along all NFs, indicating a uniform NP dispersion within the shell and the absence of agglomerates, thereby confirming the successful fabrication of a well-defined core–shell architecture (Fig. 3D).

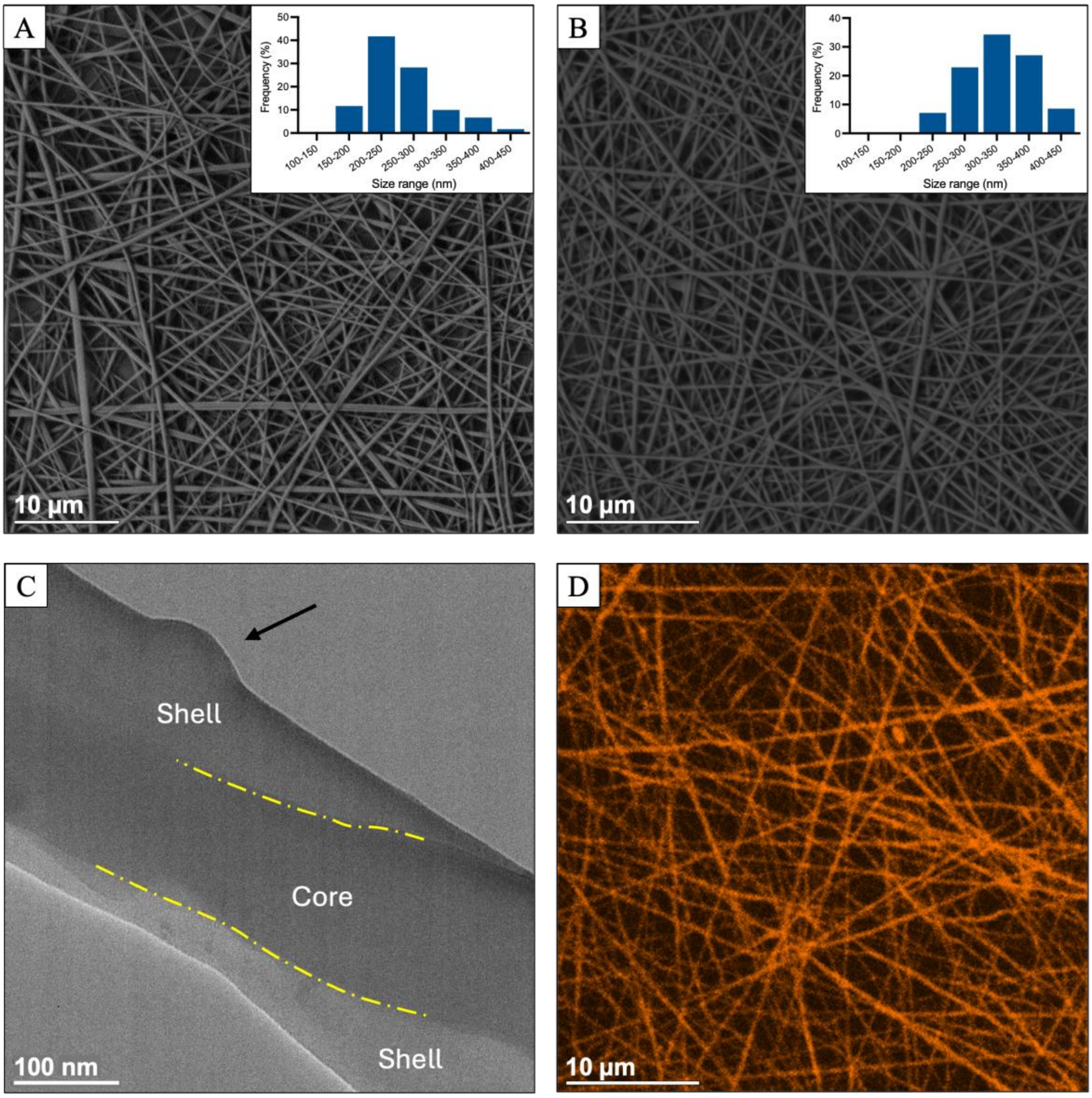

Figure 3. SEM micrographs and corresponding NFs diameter distribution histograms (insets) of (A) control NFs (Nf_CS15a) and (B) NPs-loaded NFs (Nf_CS15a-NPs); (C) TEM image highlighting the core–shell structure of the NFs: (D) *CLSM* images of NF_CS15a loaded with fluorescent PLGA:poloxamer NPs in the shell. The homogeneous red fluorescence observed along the NFs indicates uniform NP distribution and the absence of agglomerates, confirming the successful formation of a well-defined core–shell structure.

3.4. Chemical-physical Characterization of Electrospun Nanofibers

Infrared spectroscopy is an effective analytical technique to investigate the interactions between components within complex structures such as core–shell NFs. FTIR-ATR is highly sensitive to hydrogen bonding, whose formation can be identified by the characteristic red shift to lower wavenumbers in the vibrational bands in the involved functional groups. Fig. 4A shows the FTIR-ATR spectra of core-shell NFs with and without NPs, compared with the spectra of the raw materials, HA and PVP. The spectra of HA exhibited all characteristic bands and peaks associated with polysaccharides. The strong absorption bands observed in the 900–1200 cm⁻¹ range correspond to the C-O, C-O-C glycosidic and C-O-H bonds vibrations. In the HA spectra, a broad band around 3300 cm⁻¹ corresponds to the stretching vibrations of hydroxyl groups (O–H) overlapping with N–H stretching bands. The carbonyl (C=O) stretching vibrations of the carboxylate group were observed at approximately 1605 cm⁻¹ and 1405 cm⁻¹. For PVP, the spectra exhibited a prominent band at 1666 cm⁻¹, corresponding to the stretching vibrations of the carbonyl group (C=O) within the pyrrolidone ring and the band at 1425 cm⁻¹ was assigned to CH_2/CH_3 deformation and pyrrolidone-ring deformation of PVP (aliphatic C–H bending in the 1450–1400 cm⁻¹ region). Analyses of HA/PVP blend spectra suggest the presence of intermolecular interactions between polymer chains. These interactions likely involved the hydroxyl and carboxylate groups of HA and the carbonyl group of PVP. Notably, shifts in the corresponding peaks are also evident in the spectra of the core–shell NFs, indicating the formation of hydrogen bonds within the shell polymers. The FTIR analysis confirmed the intermolecular interactions between polymer chains that impact the viscosity behavior and mechanical properties.[58] At the same time, the spectra of Nf_CS1a and Nf_CS15a-NPs exhibited no noticeable difference, suggesting the absence of interactions between the shell polymers and the NPs.

Thermal stability of Nf_CS15a and Nf_CS15a-NPs, PLGA NPs and HA were investigated through TGA measurements and reported in Fig. 4B. All NF samples exhibited initial decomposition temperatures above 200 °C, indicating adequate thermal stability for potential use in biomedical applications. The degradation onset temperature (T_{onset}) and the temperature at maximum degradation rate ($T_{max.deg.rate}$), defined as the maximum of the weight loss derivative curves, were determined for all samples. Drug-loaded NFs showed a three-step thermal degradation process. The initial weight loss, occurring up to approximately 100°C, was attributed to the evaporation of adsorbed water, a behavior typical of HA due to its strong hydrophilicity. Following this, two major degradation events were observed starting at 182°C and 361°C for Nf_CS15a, while for Nf_CS15a-NPs, the corresponding onsets were at 182°C and 392°C. In both cases, the degradation peaks reached their maximum at 282°C and 435°C, respectively. According to literature data, PVA undergoes substantial weight loss within the temperature range of 216 to 320°C with a maximum at approximately 278°C.[59, 60] In contrast, PVP exhibits a single-step degradation process starting at 394°C with maximum rate decomposition temperature around 480°C. Concerning the HA curve, it is evident that there was a first water evaporation step and a characteristic two-stage polysaccharide degradation starting at 204 °C and at 300 °C.[61, 62]

The degradation curve of PLGA consisted of one single step located around 200°C (depending on the PLA-PGA ratio).[63] Considering the degradation temperatures of fibers, it is possible to assume that the presence of the shell matrix slightly hinders the degradation process of NPs and HA.

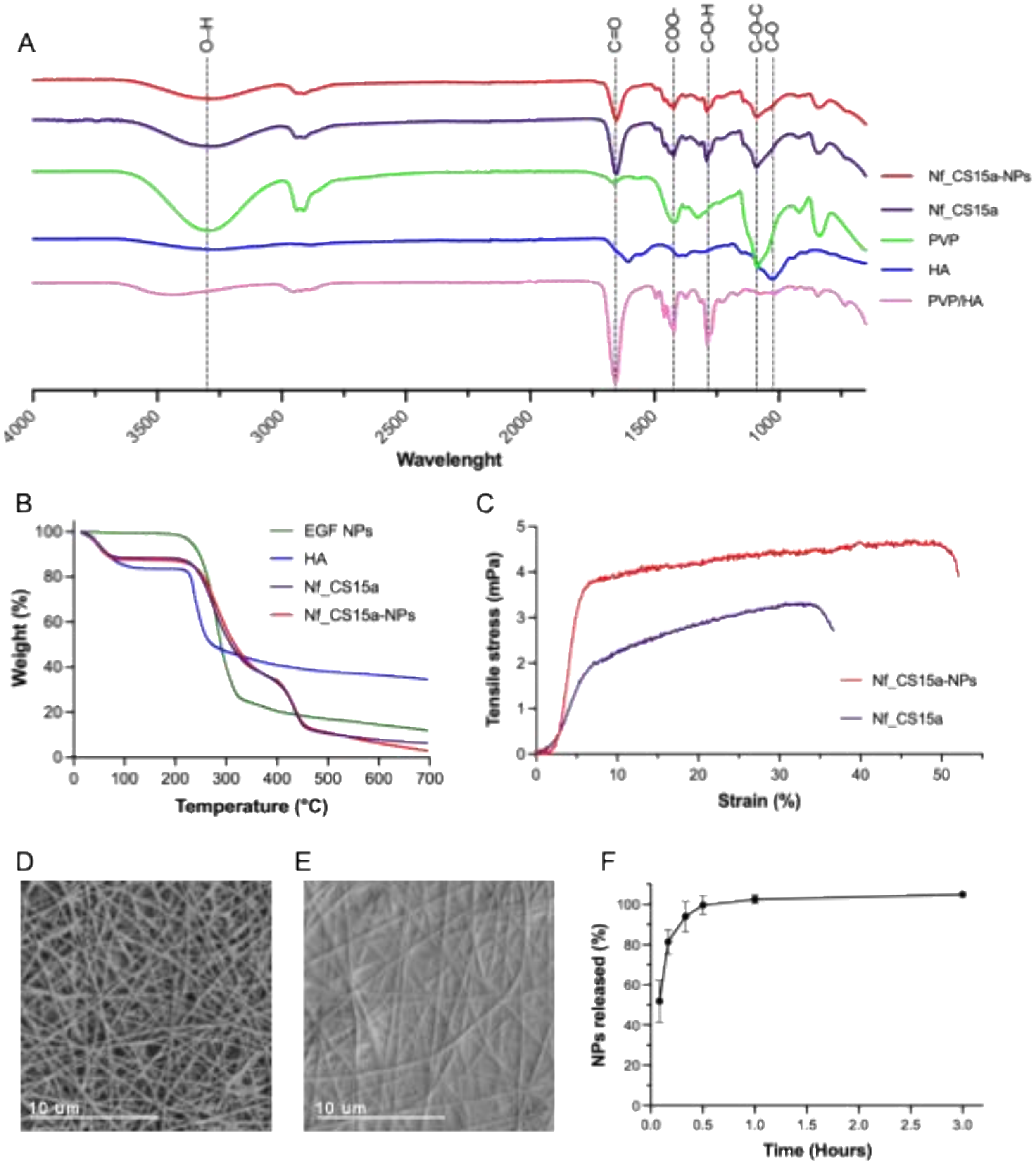

Figure 4. (A) FTIR-ATR spectra of PVP, HA, their combination used for NFs preparation, control NFs (Nf_CS15a), and NFs containing EGF-loaded NPs and Cip (Nf_CS15a-NPs); (B) representative stress-strain curve of Nf samples; (C) TGA thermograms of HA, EGF-loaded NPs, control NFs (Nf_CS15a), and drug-loaded NFs (Nf_CS15a-NPs); (D) SEM image of NFs before and (E) after contact with water; (F) release profile of NPs-Rhod in PBS from the core–shell NFs mat. The fast release observed suggests that the rapid dissolution of the NFs shell facilitates efficient NPs diffusion and enhances dispersion in the aqueous medium.

The resistance of NF mats to a force tending to tear them apart is an important factor for wound dressing applications, as well as for handling and storage. In this context, NFs with and without NPs showed an elastic response followed by a plastic deformation up to failure (Fig. 4C). This behavior is influenced by the presence of NPs, which slightly enhanced the mechanical properties of the samples by increasing both the elastic modulus and the strain at break, indicating improved mechanical performance due to a reinforcing effect. The role of PLGA in enhancing the stiffness and mechanical integrity of NFs is well established, and it is frequently used in polymer blends to produce stable electrospun mats.[8, 64, 65] This study further demonstrates that PLGA NPs can also provide additional structural reinforcement, improving the mechanical stability of the NFs. To quantitatively assess the mechanical performance, Young's modulus, maximum stress, and elongation at break were measured, representing the mats' ability to withstand tensile forces without tearing. The corresponding values are reported in Table 2. The results indicated that the mechanical performance of the proposed systems falls within the range reported in the literature for other electrospun membranes for wound healing, as well as natural skin.[16] In fact, Young's modulus of the human skin varies between 4.6 and 20 MPa for the extension tests, depending on several factors such as age, skin color, previous lesions and genetic factors [66]. The proposed drug-loaded NFs demonstrated high strain at break and maximum stress values, indicating sufficient durability to resist tearing during handling and storage.

Table 2. Stress at peak (σ peak), strain at break (ε break), and Young's modulus (E) of NFs samples. The results are reported as the average of at least five independent experiments ± standard deviation (SD).

Sample	***σ peak (MPa)***	***ε break (%)***	***E (MPa)***
Nf_CS15a	3.7 ± 0.4	39.3 ± 8.9	6.2 ± 2.3
Nf_CS15a-NPs	4.5 ± 1.0	62.6 ± 3.7	10.0 ± 3.5

An insight into the core-shell behavior of NFs in contact with water was provided (Fig. 4D-E). As expected, the contact of the electrospun NFs mat with a water droplet revealed that the shell polymers (PVP-HA), being water-soluble, dissolved rapidly, whereas the core (PVA) preserved its structure. Although all the polymers used for the core and shell are hydrophilic, their water solubility is indeed markedly different: PVP and HA readily dissolve in aqueous environments, while fully hydrated PVA remains stable at room temperature and dissolves only at temperatures exceeding 80°C. PVA-based fibrous systems have been reported to retain sufficient structural stability on the wound bed within clinically relevant dressing change intervals, thereby supporting sustained drug release and therapeutic activity.[44, 46, 48] Therefore, the core was able to maintain structural integrity over a more prolonged period to allow controlled release of the loaded CIP as well as providing exudate control including providing an ideal moist environment that prevents both drying out and excessive collection of exudate. By dissolving rapidly, the shell polymers enable efficient drug release and increases their dispersion in aqueous environments.[67] This result is consistent with the release profile of EGF-loaded NPs from the polymeric NFs (Fig. 4F), which exhibited a rapid initial release with sustained delivery over time. This burst-like behavior further supports the localization of most NPs in the shell part of the system, allowing for their quick diffusion into the surrounding area shortly after application, with minimal retention within the inner structure of the matrix. Finally, the presence of PVP further enhances NP dispersion in aqueous environments due to its surfactant-like behavior.[68]

3.5. *In Vitro* Drug Release from Nanofibers

The release of Cip and EGF from Nf_CS15a was evaluated using a release system that simulates the application of NFs to an infected wound site. Fig. 5 shows the release profiles of Cip and EGF from Nf_CS15a. The release profiles of Cip from the NFs exhibited similar trends regardless of drug loading. Notably, over 50% of the loaded Cip was released within the first 24 hours. This rapid initial release could be beneficial for providing an immediate antibacterial effect at the start of treatment. However, core-shell NFs also sustained Cip release for up to six days, ensuring a prolonged therapeutic concentration at the application site. The release profile of EGF followed a biphasic trend, with an initial rapid release of approximately 20% within the first 24 hours, followed by a controlled release lasting up to 14 days. This pattern indicates that the initial burst results from the solubilization of the NFs outer layer which subsequently releases EGF in this layer and on the surface of the NPs. On the other hand, the prolonged release was governed by the gradual degradation of the polymeric PLGA NPs to release the remaining encapsulated EGF locally at the wound site and extending for at least two weeks. Sustained GFs delivery at the wound site is highly beneficial, as it continuously stimulates fibroblast proliferation and accelerates wound healing. Additionally, localized EGF release restricts uncontrolled diffusion away from the wounded tissue and enables prolonged stimulation of fibroblast proliferation and tissue regeneration which is highly beneficial for effective wound healing, whilst at the same time minimizes side effects and reduces exposure to non-target tissues.[6]

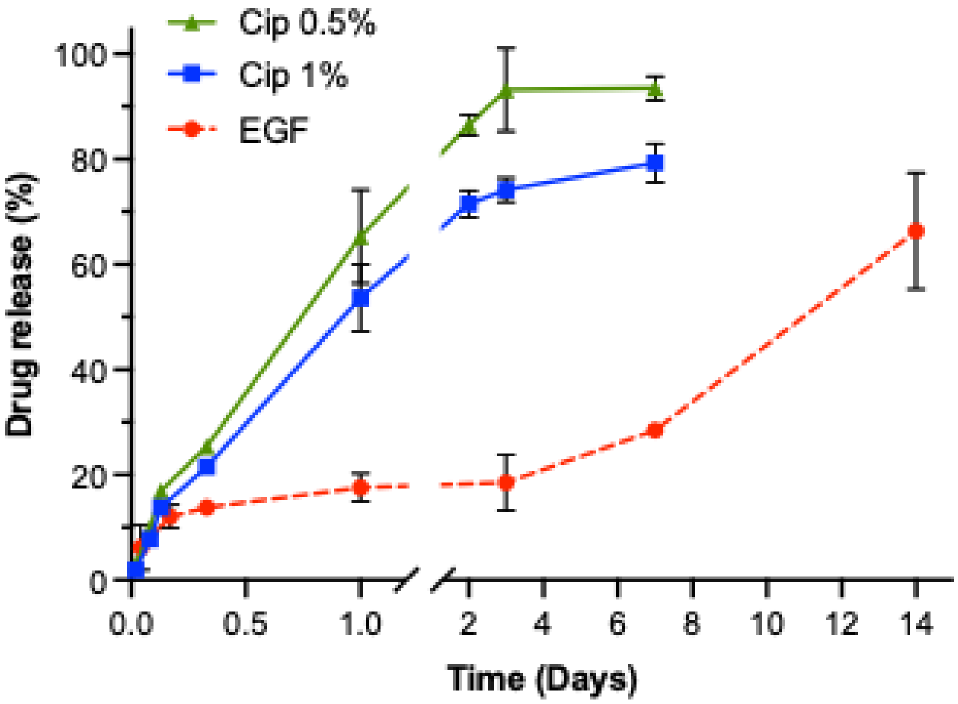

Figure 5. Release profiles of Cip (solid lines) and EGF (dotted line) from NFs in simulated wound fluid (SWF, pH 7.4), evaluated using a release setup mimicking NFs application to a wound site. Results are expressed as the percentage of EGF or Cip released (mean ± standard deviation, n = 3), based on measurements from three independent NFs samples.

3.6. Antimicrobial Activity

The results of the disk diffusion assay are presented in Fig. 6, which includes a representative bar graph of inhibition zone diameters (A), alongside photographic documentation of the plates (B) at 24 and 48 hours. Cip-loaded NFs (0.5% and 1% w/w) showed clear inhibition halos against all tested bacterial strains, whereas unloaded NFs (0%) did not display any antimicrobial effect. Control filter paper disks impregnated with 2.2 µg and 4.4 µg of Cip solution in water similarly produced distinct zones of inhibition, confirming the responsiveness of the assay system (supplementary material S3).

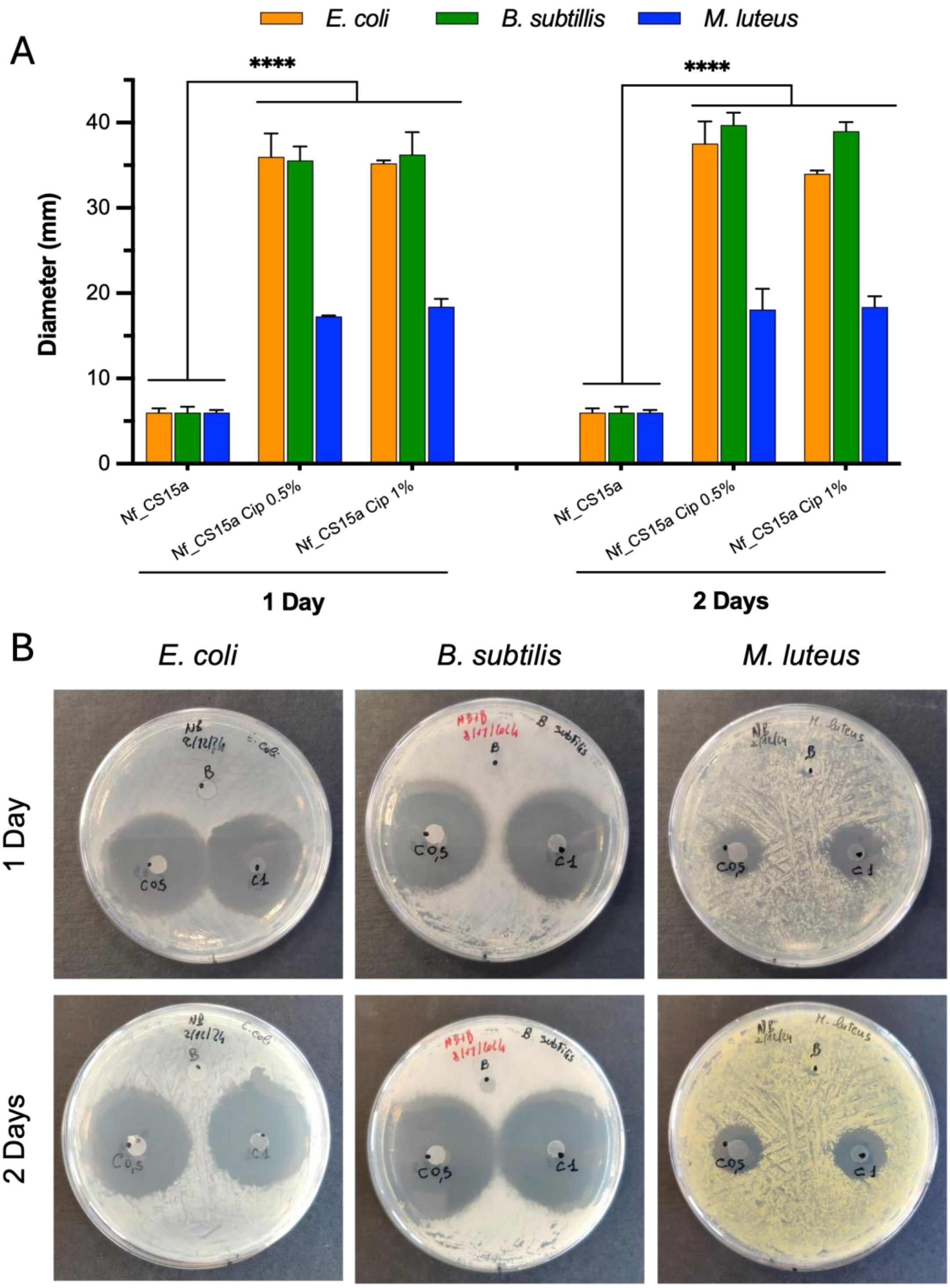

Figure 6. Antimicrobial activity of Cip-loaded NFs. (A) average inhibition zone diameters (± SD) at 24 and 48 hours for NFs loaded with 0.5% and 1% w/w Cip. (B) representative photographs of NB-agar plates seeded with *E. coli* DSM 498, *M. luteus* DSM 348, and *B. subtilis* subsp. *spizizenii* DSM 347, showing inhibition halos around NFs and control disks at 24 hours and 48 hours. The statistical significance was calculated using a one-way ANOVA test on GraphPad Prism 10 (****: $p<0.0001$).

No significant difference in halo diameter was observed between the NFs loaded at 0.5% and 1% w/w, suggesting that a plateau in antimicrobial efficacy may have been reached under the tested conditions. The comparable efficacy of the 0.5% and 1% w/w formulations suggests that the lower Cip loading already achieved a maximum antimicrobial response under the tested conditions. The inhibition zones produced by the drug-loaded NFs were comparable in size to those of the corresponding Cip-loaded filter paper controls, indicating effective release and bioactivity of the incorporated antibiotic from the polymeric matrix. These results highlight the potential of the NF matrix for sustained local antibiotic delivery. Cip, a broad-spectrum antibiotic with strong activity against Gram-negative and selected Gram-positive bacteria, showed the expected efficacy against all three tested strains, each of which proved susceptible to the drug. The largest and comparable inhibition zones were recorded for *E. coli* and *B. subtilis*, while *M. luteus* exhibited smaller halos, indicating lower sensitivity under the tested conditions. In all cases, inhibition zones persisted after 48 hours, with slight differences in diameter depending on the bacterial species and the type of disk employed.

3.7. Biocompatibility Studies of Nanofiber Membranes

3.7.1. Hemolysis assay

Hemolysis assays provide a simple and reliable method to assess the hemocompatibility of drug-loaded core–shell NFs. Ensuring hemocompatibility is essential when evaluating biomaterials for wound dressing applications.[37, 69, 70] The hemolytic properties of the nanofibrous mats presented in Fig. 7A-B showed that the hemolysis index for all samples was below 0.5%, indicating that the nanofibrous mats can be classified as non-hemolytic materials. According to the ASTM F756-17 (2017) standard, materials with a hemolysis rate below 2% are considered non-hemolytic, while those exceeding this threshold are classified as hemolytic.[71] These findings confirmed that the tested NFs exhibit excellent hemocompatibility, as lower hemolysis values correspond to greater red blood cell safety.

3.7.2. Cell viability assays

Two complementary assays were employed to assess the cytotoxicity of the drug-loaded NFs. The MTT assay provided a quantitative measure of cell metabolic activity, while the Live/Dead assay offered qualitative confirmation through fluorescence-based visualization of live and dead cells. This dual approach strengthens the reliability of biocompatibility assessment for biomaterials. Both assays revealed distinct patterns across treatment groups over the 72-hour experimental period (Fig. 7C-D), primarily influenced by the presence of Cip. After 24 hours, the control samples (cells/media only, control NFs and NFs loaded with control NPs) demonstrated optimal cellular conditions, with the control NFs and the NFs containing control NPs, and EGF NPs exhibiting excellent cell viabilities, indicating biocompatible materials that support normal cellular metabolism and homeostasis.[72, 73] The MTT assay revealed that Cip monotherapy significantly ($p<0.05$) reduced the cell viability to approximately 82%, reflecting fluoroquinolone-mediated DNA gyrase inhibition and subsequent apoptotic cascades (Fig. 7C).[74] In contrast, treatments containing EGF NPs supported higher cell proliferation, with viabilities exceeding 119% and 109% respectively, probably reflecting EGF potent mitogenic effects through EGFR-mediated activation of downstream proliferation pathways.[75] Across 48 and 72 hours, overall cell metabolic activity decreased, with Cip-only NFs showing persistent cytotoxicity (~80%), consistent with the well-documented inhibitory effects of fluoroquinolones on mammalian cells [74]. Interestingly, co-delivery with EGF NPs mitigated this effect, supporting the hypothesis that EGF not only promotes proliferation but can also counteract antibiotic-induced stress, thereby enhancing the therapeutic potential of the combination.[75]

Consistent with MTT assay results, the Live/Dead assay showed that Cip NFs monotherapy progressively reduced cell viability, from 95.48% at 24 hours to 89.90% at 48 hours and 86.71% at 72 hours (Fig. 7D). However, differences between groups, including those containing EGF NPs, were less pronounced in the Live/Dead assay, likely reflecting its more qualitative nature compared to the quantitative sensitivity of the MTT assay.

Co-delivery of Cip with EGF-loaded NPs suggests a potential clinical benefit, as EGF may mitigate antibiotic-related cellular damage during prolonged treatments without promoting excessive cell proliferation that could carry oncogenic risks. However, this protective effect appears to be time-dependent and possibly limited. Importantly, all tested dressings showed cell viability values above 70%, meeting ISO requirements for biocompatibility and confirming their safety for biomedical applications. Future studies extending the evaluation period to 7–14 days and repeating in an in vivo model will be important to determine how frequently the NFs mats should be replaced.

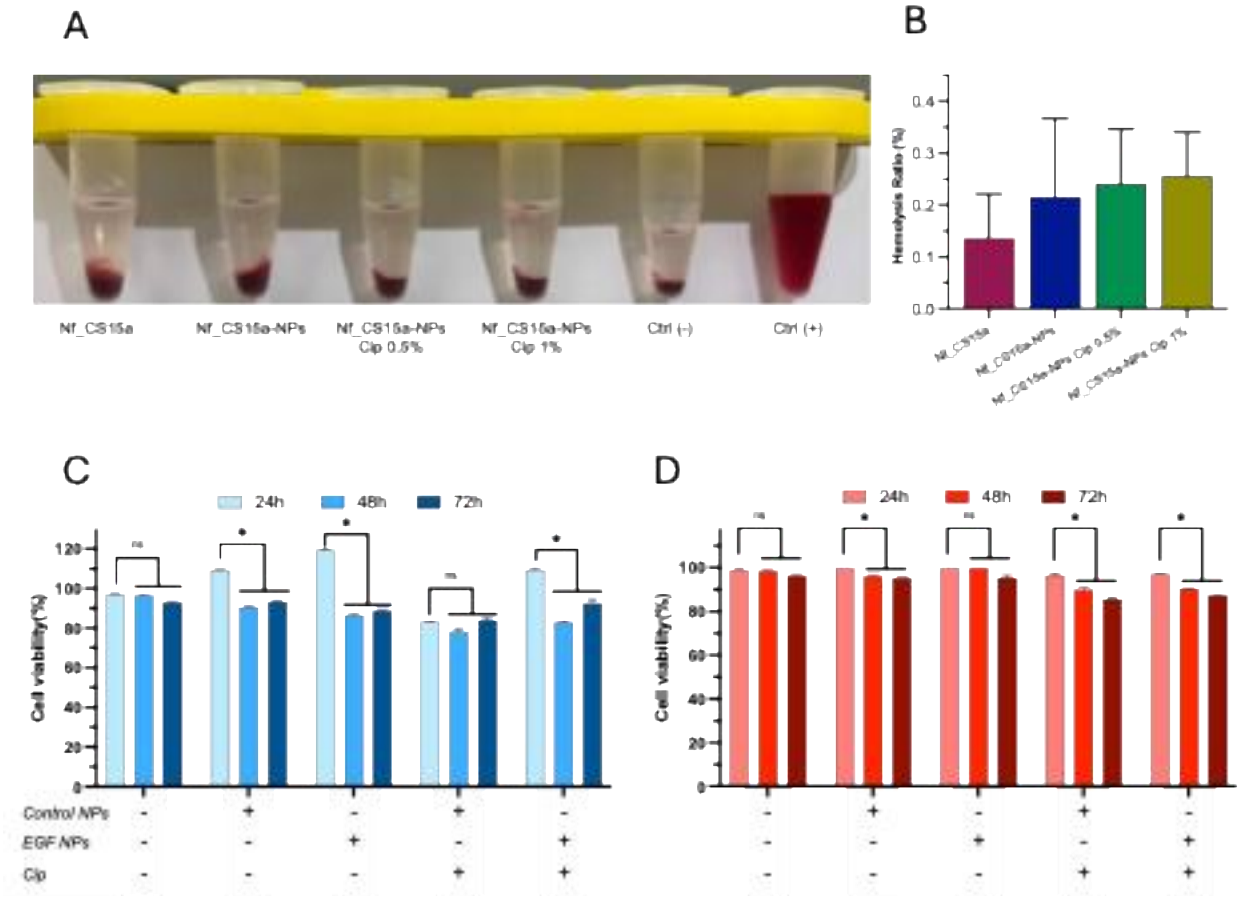

Figure 7. A) Photograph of human red blood cell dispersions exposed to different drug loaded NFs mats. B) hemolysis ratio calculated according to ASTM F756–08. All samples showed hemolysis rates below 2%, classifying them as non-hemolytic and indicating good blood compatibility for potential biomedical applications. C) MTT cell viability assay and D) live and dead assay of the Cip and NPs-loaded core–shell NFs. Each result represents the mean of three biological replicates (n = 3) with the error bars representing the Standard Deviation (± SD) (*: $p<0.05$; **: $p<0.01$). The table below the graph indicates the composition of each treatment group. The symbol "+" denotes the presence of the corresponding component in the sample, while "–" indicates its absence.

3.8. *In Vitro* Wound Healing (Scratch) Assay

The scratch assay (Fig. 8, Supplementary Materials S4) was performed to evaluate the effects of the NF dressings components on cell proliferation and migration, two key processes in wound closure, over three time points (24, 48, and 72 hours). In general, wound closure rates increased over time for all the dressings with significant differences between the rates at 24 and 72 hours, as expected. During the initial 24-hour period, all treatment groups demonstrated modest wound closure rates. No effect on gap closure was observed for the control NPs containing Hp and BSA, indicating that these components did not influence cell migration under the tested conditions. Among the tested groups, the empty

NFs (used as control dressing) and Nf_CS15a loaded with Cip and EGF-NPs achieved the highest gap closure percentages (40.7 ± 0.6% and 48.3 ± 0.8%, respectively) whereas the samples loaded with Cip showed the lowest gap closure percentage of 28.7 ± 0.6%. Cip has been previously shown to inhibit cell proliferation and migration *in vitro*, both of which are critical for wound closure, significantly reducing cell migration compared to untreated controls.[76-78] In our study, we observed significant differences in wound closure between the NFs loaded with Cip and those loaded with Cip + EGF NPs as early as 24 hours, supporting the notion that Cip alone has limited effectiveness as a wound-healing agent, particularly in the absence of infection [74]. This difference slightly decreased over time; however, the effect of Cip on gap closure remained significant after 48 and 72 hours, suggesting that the presence of EGF can at least partially counteract the detrimental effects of Cip on cell migration and promote tissue repair over time. In a similar study performed by Ahmed and coworkers, it was observed that film and wafer dressings combining Cip and fluconazole demonstrated percentage wound closure of 65.0 ± 0.2% and 67.6 ± 6.7% respectively, after exposure to keratinocytes for 7 days.[38] Their drug loaded dressings exhibited lower rates of wound closure compared to the unloaded one, which they attributed to the drug–cell interactions causing partial cell death and cell detachment, ultimately impairing wound closure. They concluded that though both drugs were useful to prevent and treat infection, the doses needed to be tuned to levels that are not toxic to human cell.

Consistently, our results showed that Cip-loaded NFs exhibited lower gap closure percentages compared to all other tested dressings; however, the addition of EGF-loaded NPs mitigated this inhibitory effect, enhancing cell migration and wound closure. The enhancement in cell proliferation correlates to the sustained release profile of EGF from PLGA NPs, which are designed to protect and gradually deliver structurally labile GFs. The release kinetics demonstrated that less than 20% of EGF was liberated within the first three days, while more than 70% was released between days 4 and 14, a time frame that likely aligns more closely with the proliferative and remodeling phases of wound healing. This observation seems to confirm the importance of time and target-driven drug delivery to chronic wound sites to ensure that the desired therapeutic outcomes are achieved.[6] This is important as it suggests that core-shell NPs embedding GFs, could be a feasible approach to chronic wound healing, whilst also reducing the potential cytotoxicity of co-administered antibiotics in the case of infected chronic wounds such as diabetic foot ulcers, where systemic administration of antibiotics can be ineffective due to poor blood circulation in the foot regions.

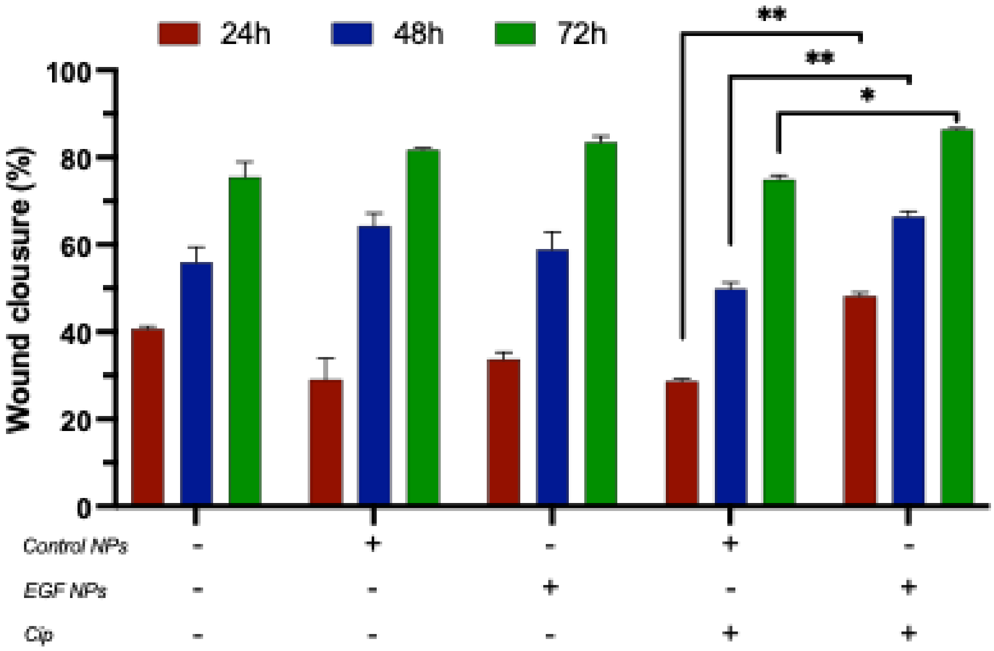

Figure 8. *In vitro* wound healing (scratch) assay of the Cip and NPs-loaded NFs. Each result represents the mean of three biological replicates (n = 3) with the error bars representing the Standard Deviation (± SD). Significant differences (*: $p<0.05$; **: $p<0.01$) were observed between Nf_CS15a loaded with Cip alone and Nf_CS15a loaded with Cip and EGF NPs. The table below the graph indicates the composition of each treatment group. The symbol "+" denotes the presence of the corresponding component in the NF, while "–" indicates its absence.

4. CONCLUSION

In this work, we have successfully demonstrated how the integration of complementary nanoencapsulation strategies can be harnessed to develop an advanced multifunctional wound dressing. Leveraging the versatility, structural precision, and cost-effectiveness of electrospinning, core–shell NFs with a PVA core and a PVP/HA shell were obtained. The rapid dissolution of the PVP/HA shell enabled the immediate release of EGF-loaded NPs, delivering regenerative cues directly to the wound bed, while simultaneously exposing the underlying PVA core, which absorbs wound exudate and subsequently triggers the controlled release of Cip. The combined release of Cip and EGF-loaded NPs is expected to act simultaneously on multiple underlying causes of chronic wounds, offering potential for improved clinical outcomes. The modified disk diffusion assay confirmed effective antimicrobial activity of the developed core–shell NFs against both Gram-positive and Gram-negative reference strains, while the absence of inhibition zones around unloaded NFs validated the specificity of the drug-mediated effect. Biocompatibility studies confirmed that the NFs membranes are safe for biomedical use, maintaining cell viability above 70%, and meeting ISO standards. EGF exerted a time-dependent protective effect against antibiotic-induced cellular damage without triggering excessive proliferation. While Cip-loaded NFs impaired gap closure, co-delivery with EGF-loaded NPs restored proliferation, consistent with EGF sustained release during key wound healing phases.

Overall, the proposed core-shell architecture integrates rapid dissolution and exudate absorption with sustained, targeted delivery of therapeutic agents, providing a multifunctional platform tailored to the complex demands of chronic wound repair. These findings highlight the potential of core–shell NFs as a versatile platform for tackling key challenges in chronic wound healing. By combining immediate antimicrobial action with sustained regenerative signaling, this multifunctional dressing offers a synergistic approach to promote tissue repair. Such a strategy holds significant promise for improving outcomes in chronic wounds, including poorly vascularized conditions such as diabetic foot ulcers, and represents a step forward toward more effective, multifunctional therapeutic solutions. Future studies involving *in vivo* animal testing will confirm this initial proof of concept and provide opportunity for potential clinical translation.

ACKNOWLEDGEMENT

This work was supported by The Royal Society as part of the UK-Italy International Exchanges Grants Scheme 2021. The authors gratefully acknowledge Prof. Mariano Stornaiuolo for his valuable support in the confocal microscopy analysis.

AUTHOR CONTRIBUTIONS

Ovidio Catanzano: conceptualization, data curation, formal analysis, methodology, investigation, writing – original draft; **Irene Bonadies:** data curation, formal analysis, investigation, writing – review and editing; **Clara Gamba:** investigation; **Michele Guida**: investigation; **Gennaro Roberto Abbamondi**: data curation, formal analysis, investigation; **Giuseppina Tommonaro:** data curation, formal analysis, investigation; **Hossam Ahmed:** investigation, formal analysis, writing – original draft; **Fabiana Quaglia:** conceptualization, supervision, resources, funding acquisition, writing – review and editing; **Joshua S. Boateng:** conceptualization, supervision, resources, funding acquisition, writing – review and editing.

All authors have given approval to the final version of the manuscript.

CONFLICT OF INTEREST DISCLOSURES

The authors declare no competing financial interest.

DECLARATION OF GENERATIVE AI AND AI-ASSISTED TECHNOLOGIES IN THE MANUSCRIPT PREPARATION PROCESS

During the preparation of this work the authors used ChatGPT (OpenAI) in order to assist with the refinement of grammar and syntax. After using this tool, the authors reviewed and edited the content as needed and take(s) full responsibility for the content of the published article.

REFERENCES

1. J. Boateng and O. Catanzano, *J Pharm Sci*, 2015, **104**, 3653-3680.
2. A. Sharma, D. Sharma and F. Zhao, *Adv. Healthcare Mater.*, 2023, **12**, 2300556.
3. Q. Zeng, X. Qi, G. Shi, M. Zhang and H. Haick, *ACS Nano*, 2022, **16**, 1708-1733.
4. A. Alberts, D.-I. Tudorache, A.-G. Niculescu and A. M. Grumezescu, *Gels*, 2025, **11**, 123.
5. Y. Yao, M. Huang, Y. Li, Y. Lin, J. Dong, J. Du, A. Zhai, C. Bi and L. Li, *Small Sci.*, 2025, **n/a**, e202500482.
6. O. Catanzano, F. Quaglia and J. S. Boateng, *Expert Opin Drug Deliv*, 2021, **18**, 1-23.
7. M. Sharma, A. Saraf, C. Bonde, S. Bonde, K. Tiwari, G. Lodha, S. Singh and V. Mishra, in *Intelligent Nanobiosystems in Medicine and Healthcare, Volume 2*, eds. V. Mishra, C. M. Hussain and Y. Mishra, Academic Press, 2025, DOI: https://doi.org/10.1016/B978-0-323-90254-0.00015-5, ch. 15, pp. 375-416.
8. H. Zhang, D. Ji, K. Zhao, Z. Li, S. Yang, P. Wang, W. Cao and Y. Sun, *Mater. Res. Express.*, 2025, **12**, 015403.
9. Y. Dong, S. Fu, J. Yu, X. Li and B. Ding, *Adv. Funct. Mater.* , 2024, **34**, 2311199.
10. Y. Cho, J. W. Baek, M. Sagong, S. Ahn, J. S. Nam and I.-D. Kim, *Advanced Materials*, 2025, **37**, 2500162.
11. C. A. M. Ferreira, M. F. L. Lemos, A. C. Maurício and J. R. Dias, *Polymer Reviews*, 2025, DOI: 10.1080/15583724.2025.2524625, 1-36.
12. X. Zhang, Y. Wang, Z. Gao, X. Mao, J. Cheng, L. Huang and J. Tang, *J. Appl. Polym. Sci.*, 2024, **141**, e54746.
13. Y. Liu, T. Li, Y. Han, F. Li and Y. Liu, *Curr. Opin. Biomed. Eng.*, 2021, **17**, 100247.
14. S. Zhang, W. Yang, W. Gong, Y. Lu, D.-G. Yu and P. Liu, *RSC Advances*, 2024, **14**, 14374-14391.
15. J. A. Matthews, G. E. Wnek, D. G. Simpson and G. L. Bowlin, *Biomacromolecules*, 2002, **3**, 232-238.
16. A. Li, L. Li, B. a. Zhao, X. Li, W. Liang, M. Lang, B. Cheng and J. Li, *Int. J. Biol. Macromol.*, 2022, **194**, 914-923.
17. J. Zhao, L. Chen, A. Ma, X. Bai, Y. Zeng, D. Liu, B. Liu, W. Zhang and S. Tang, *Mater. Today Bio*, 2024, **29**, 101309.
18. Y. Xu, Q. Saiding, X. Zhou, J. Wang, W. Cui and X. Chen, *Smart Medicine*, 2024, **3**, e20230034.
19. S. H. Shin, Y. G. Koh, W. G. Lee, J. Seok and K. Y. Park, *Int Wound J*, 2023, **20**, 2414-2423.

20. J. Berlanga-Acosta, A. Garcia-Ojalvo, J. Fernández-Montequin, V. Falcon-Cama, N. Acosta-Rivero, G. Guillen-Nieto, M. Pujol-Ferrer, M. Limonta-Fernandez, M. Ayala-Avila and E. Eriksson, *Int. J. Mol. Sci.*, 2024, **25**, 10883.

21. V. Sethuraman, K. Janakiraman, A. Ramesh and G. Sampath, *Regen. Eng. Transl. Med.*, 2025, DOI: 10.1007/s40883-025-00505-x.

22. O. Catanzano and J. Boateng, in *Therapeutic Dressings and Wound Healing Applications*, 2020, DOI: doi:10.1002/9781119433316.ch13, pp. 291-314.

23. G. Agarwal, S. Bhargava and S. Dumoga, *Wound Repair Regen.*, 2025, **33**, e70031.

24. S. S. Swain, V. V. S. R. Karri, G. Kuppusamy, T. K. Praveen and S. Dutta, in *Recent Advances in Nanomedicines Mediated Wound Healing*, ed. P. Kesharwani, Academic Press, 2025, DOI: https://doi.org/10.1016/B978-0-443-22027-2.00018-X, ch. 13, pp. 227-239.

25. A. Vijayan, P. P. James, C. K. Nanditha and G. S. V. Kumar, *Int J Nanomedicine*, 2019, **14**, 2253-2263.

26. P. Losi, E. Briganti, C. Errico, A. Lisella, E. Sanguinetti, F. Chiellini and G. Soldani, *Acta Bio.*, 2013, **9**, 7814-7821.

27. K. K. Chereddy, A. Lopes, S. Koussoroplis, V. Payen, C. Moia, H. Zhu, P. Sonveaux, P. Carmeliet, A. des Rieux, G. Vandermeulen and V. Préat, *Nanomed.: Nanotechnol. Biol. Med.*, 2015, **11**, 1975-1984.

28. J. Xin, Z. Yang, S. Zhang, L. Sun, X. Wang, Y. Tang, Y. Xiao, H. Huang and W. Li, *Journal of Nanobiotechnology*, 2024, **22**, 439.

29. W. Xu, T. Xu, L. Yu, X. Ning, C. Zhang, B. Yi, W. Dai, Z. Zhu and H. Zhao, *Materials Today Bio*, 2025, **34**, 102155.

30. P. Khosravian, R. Mardani, Z. K. Boldaji, M. Javdani and M. Hashemnia, *Naunyn-Schmiedeberg's Archives of Pharmacology*, 2025, DOI: 10.1007/s00210-025-04417-z.

31. L. V. Schulte-Werning, I. Laidmäe, L. M. Hemmingsen, J. Heinämäki, L. Preem, K. Kogermann and A. M. Holsæter, *European Journal of Pharmaceutical Sciences*, 2025, **214**, 107264.

32. T. Ju, S. Gaisford and G. R. Williams, *J. Drug Delivery Sci. Technol.*, 2024, **91**, 105264.

33. I. d'Angelo, M. Garcia-Fuentes, Y. Parajo, A. Welle, T. Vantus, A. Horvath, G. Bokonyi, G. Keri and M. J. Alonso, *Mol Pharm*, 2010, **7**, 1724-1733.

34. Clinical and Laboratory Standards Institute (CLSI), *Journal*, 2022.

35. A. W. Bauer, D. M. Perry and W. M. Kirby, *AMA Arch Intern Med*, 1959, **104**, 208-216.

36. J. Schindelin, C. T. Rueden, M. C. Hiner and K. W. Eliceiri, *Mol. Reprod. Dev.*, 2015, **82**, 518-529.

37. M. F. Elahi, G. Guan and L. Wang, *Rev. Adv. Mater. Sci.*, 2014, **38**, 148-159.

38. A. Ahmed, G. Getti and J. Boateng, *Int. J. Pharm.*, 2021, **606**, 120903.

39. M. Afzali, N. Esfandiaribayat and J. Boateng, *Drug Deliv. Transl. Res.*, 2025, **15**, 2483-2508.

40. B. A. Pfeffer and S. J. Fliesler, *Exp. Eye Res.*, 2017, **161**, 17-29.

41. L. G. Rodriguez, X. Wu and J.-L. Guan, in *Cell Migration: Developmental Methods and Protocols*, ed. J.-L. Guan, Humana Press, Totowa, NJ, 2005, DOI: 10.1385/1-59259-860-9:023, pp. 23-29.

42. I. Arranz-Valsero, L. Soriano-Romaní, L. García-Posadas, A. López-García and Y. Diebold, *Exp. Eye Res.*, 2014, **125**, 183-192.

43. I. Bonadies, L. Maglione, V. Ambrogi, J. D. Paccez, L. F. Zerbini, L. F. Rocha e Silva, N. S. Picanço, W. P. Tadei, I. Grafova, A. Grafov and C. Carfagna, *Eur. Polym. J.*, 2017, **89**, 211-220.

44. M. Mahmoudi, P. Alizadeh and M. Soltani, *Biomater. Adv.*, 2023, **153**, 213530.

45. A. W. Jatoi, H. Ogasawara, I. S. Kim and Q.-Q. Ni, *Mater. Lett.*, 2019, **241**, 168-171.

46. M. M. Nemati, R. Heidari, A. Keshavarzi, A. Ahmadi, M. Abedi, S. Ranjbar and Y. Ghasemi, *Appl. Biochem. Biotechnol.* , 2025, **197**, 194-215.

47. G. C. Türkoğlu, N. Khomarloo, E. Mohsenzadeh, D. N. Gospodinova, M. Neznakomova and F. Salaün, *Int J Mol Sci*, 2024, **25**.

48. F. T. Zahra, Q. Quick and R. Mu, *Polymers*, 2023, **15**, 3837.

49. O. Catanzano, V. D'Esposito, S. Acierno, M. R. Ambrosio, C. De Caro, C. Avagliano, P. Russo, R. Russo, A. Miro, F. Ungaro, A. Calignano, P. Formisano and F. Quaglia, *Carbohydr Polym*, 2015, **131**, 407-414.

50. I. d'Angelo, P. Yolanda, H. Anikó, K. György, L. R. M. Immacolata and M. J. and Alonso, *J. Microencapsul.*, 2010, **27**, 57-66.

51. N. Csaba, A. Sánchez and M. J. Alonso, *J. Control. Release*, 2006, **113**, 164-172.

52. L. Mayol, C. Serri, C. Menale, S. Crispi, M. T. Piccolo, L. Mita, S. Giarra, M. Forte, A. Saija, M. Biondi and D. G. Mita, *Eur. J. Pharm. Biopharm.*, 2015, **93**, 37-45.

53. F. Madani, H. Morovvati, T. J. Webster, S. Najaf Asaadi, S. M. Rezayat, M. Hadjighassem, M. Khosravani and M. Adabi, *Sci. Rep.*, 2024, **14**, 19516.

54. C. Borselli, F. Ungaro, O. Oliviero, I. d'Angelo, F. Quaglia, M. I. La Rotonda and P. A. Netti, *J. Biomed. Mater. Res. A*, 2010, **92A**, 94-102.

55. B. Mulloy and R. J. Linhardt, *Curr. Opin. Struct. Biol.*, 2001, **11**, 623-628.

56. Y. Feng, Q. Li, D. Wu, Y. Niu, C. Yang, L. Dong and C. Wang, *Biomaterials*, 2017, **134**, 128-142.

57. T. Jamnongkan, R. Shirota, S. K. Sukumaran, M. Sugimoto and K. Koyama, *Polym. Eng. Sci.*, 2014, **54**, 1969-1975.

58. K. Lewandowska and M. Szulc, *Molecules*, 2021, **26**, 5233.

59. M. I. Loría-Bastarrachea, W. Herrera-Kao, J. V. Cauich-Rodríguez, J. M. Cervantes-Uc, H. Vázquez-Torres and A. Ávila-Ortega, *J. Therm. Anal. Calorim.*, 2011, **104**, 737-742.

60. G. S. A. Suleiman, X. Zeng, R. Chakma, I. Y. Wakai and Y. Feng, *Polym. Adv. Technol.*, 2024, **35**, e6327.

61. W. R. de Souza, B. V. Quevedo, P. S. Garcia, L. C. S. C. da Silva, D. Komatsu and E. A. de Rezende Duek, *Polymer Bulletin*, 2025, **82**, 1915-1933.

62. L. Lapčík, Otyepková, E., Lapčíková, B., Otyepka, M., Vlček, J., & Kupská, I. , in *Hyaluronic Acid for Biomedical and Pharmaceutical Applications*, ed. M. N. Collins, Smithers Rapra, 2014.

63. J. Palacios, C. Albano, G. González, R. V. Castillo, A. Karam and M. Covis, *Polym. Eng. Sci.*, 2013, **53**, 1414-1429.

64. T. Eren Böncü and N. Ozdemir, *Beilstein J. Nanotechnol.* , 2022, **13**, 245-254.

65. Z. X. Meng, X. X. Xu, W. Zheng, H. M. Zhou, L. Li, Y. F. Zheng and X. Lou, *Colloids Surf., B*, 2011, **84**, 97-102.

66. H. Zahouani, C. Pailler-Mattei, B. Sohm, R. Vargiolu, V. Cenizo and R. Debret, *Skin Res Technol*, 2009, **15**, 68-76.

67. A. Martin, J. N. Nyman, R. Reinholdt, J. Cai, A.-L. Schaedel, M. J. A. van der Plas, M. Malmsten, T. Rades and A. Heinz, *Nanomaterials*, 2022, **12**, 2437.

68. Y. Shahzad, S. N. H. Shah, M. T. Ansari, R. Riaz, A. Safdar, T. Hussain and M. Malik, *Chin. Sci. Bull.*, 2012, **57**, 1685-1692.

69. X. Zhai, Z. Cui, Y. Li, S. Hou and W. Shen, *Heliyon*, 2022, **8**, e12063.

70. S. Todros, M. Todesco and A. Bagno, *Processes*, 2021, **9**, 1949.

71. ASTM International, *Journal*, 2017, DOI: 10.1520/F0756-17.

72. S. Peters, S. Zimmermann and A. A. Adjei, *Cancer Treat Rev*, 2014, **40**, 917-926.

73. Ralph J. DeBerardinis and Craig B. Thompson, *Cell*, 2012, **148**, 1132-1144.

74. P. C. Sharma, A. Jain, S. Jain, R. Pahwa and M. S. Yar, *J. Enzyme Inhib. Med. Chem.*, 2010, **25**, 577-589.

75. J. Berlanga-Acosta, J. Gavilondo-Cowley, P. López-Saura, T. González-López, M. D. Castro-Santana, E. López-Mola, G. Guillén-Nieto and L. Herrera-Martinez, *Int Wound J*, 2009, **6**, 331-346.

76. M. F. Sanchez, M. L. Guzman, J. Flores-Martín, M. Cruz Del Puerto, C. Laino, E. A. Soria, A. C. Donadio, S. Genti-Raimondi and M. E. Olivera, *Sci. Rep.*, 2022, **12**, 16035.

77. T.-C. Chen, T.-Y. Tsai and S.-W. Chang, *Exp. Eye Res.*, 2016, **145**, 10-16.

78. M. Gouzos, M. Ramezanpour, A. Bassiouni, A. J. Psaltis, P. J. Wormald and S. Vreugde, *Front. Cell. Infect. Microbiol.*, 2020, **Volume 10 - 2020**.